GEOPHYSICS, VOL. 86, NO. 6 (NOVEMBER-DECEMBER 2021); P. H43–H52, 11 FIGS.
10.1190/GEO2020-0222.1

DOI:10.1190/geo2020-0222.1

A sliced-3D approach to finite-difference time-domain modeling by optimizing perfectly matched layers

Richard Delf[1], Antonios Giannopoulos[2], Robert G. Bingham[1], and Andrew Curtis[1]

ABSTRACT

Finite-difference time-domain forward modeling is often used to gain a more quantitative understanding of the interactions between electromagnetic fields and targets. To undertake full 3D simulations, the computational demands are challenging, so simulations are often undertaken in two dimensions, in which assumptions in the propagation of electromagnetic fields and source type can result in errors. We have developed the concept of a sliced-3D simulation, wherein a thin slice of a 3D domain with strictly 2D geometry is used to minimize computational demands while obtaining synthetic waveforms that contain full 3D propagation effects. This approach requires optimization of perfectly matched layer (PML) boundary condition parameters so as to minimize the errors associated with the source being located close to the boundary, and as a result of grazing-incident angle wave conversion to evanescent energy. We explore the frequency dependence of PML parameters, and we establish a relationship between complex frequency stretching parameters and effective wavelength. The resultant parameter choice is shown to minimize propagation errors in the context of a simple radioglaciological model, in which 3D domains may be prohibitively large, and for a near-surface cross-borehole survey configuration, a case in which full-waveform inversion may typically be used.

INTRODUCTION

Finite-difference time-domain (FDTD) forward modeling has been used in many areas of exploration and near-surface geophysics to test the performance of novel processing algorithms and acquisition (Versteeg, 1993; Langhammer et al., 2017), in data processing directly for finite difference and reverse time migration (Fisher et al., 1992; Leuschen and Plumb, 2001; Yilmaz, 2001; Church et al., 2018), and as a part of inversion algorithms including full-waveform inversion (FWI) (Virieux and Operto, 2009; Busch et al., 2012; Mozaffari et al., 2016). In electromagnetic applications, 2D formulations of the Yee algorithm (Yee, 1966) are generally used, which make the implicit assumption of lateral model invariance. The resultant synthetic 2D data have an incorrect amplitude scaling with traveltime for which a correction must be made. Many studies have used a Bleistein filter (Bleistein, 1986; Auer et al., 2013) in preprocessing of field data to facilitate comparison with 2D models (Mozaffari et al., 2016; Klotzsche et al., 2019), but it has been demonstrated that this can result in errors after the first-break arrivals or in complex velocity models (Auer et al., 2013).

Reduction to 2D requires assuming that the radar antennas are either crossline or inline, modes that are typically and hereafter denoted as TMz and TEz, respectively. The most commonly used modeling platforms apply TMz reduction from the principle that crossline antennas are more widely used in many fields. However, the importance of source polarization has been noted in several areas of the literature, including in glaciology (Langhammer et al., 2017), where the TEz mode is more commonly applied in ground-based studies (e.g., Bingham et al., 2017). To address the issues outlined above, 3D modeling must be developed, yet the computational demands are intense; therefore, there is a need to develop a computationally efficient approach for modeling 3D fields.

In this paper, we seek to minimize the computational cost of full FDTD modeling of 2D geometries using a sliced-3D approach in gprMax, an open-source ground-penetrating radar (GPR) modeling package (Warren et al., 2016). To do so, we must optimize the boundary conditions, implemented by perfectly matched layers (PMLs) so as to attenuate noise due to grazing-wave interactions with the model boundaries. We investigate the frequency dependence of PML performance for the sliced-3D application, and we demonstrate

Manuscript received by the Editor 10 April 2020; revised manuscript received 29 April 2021; published ahead of production 24 August 2021; published online 01 October 2021.
[1]University of Edinburgh, School of GeoSciences, Edinburgh EH8 9XP, UK. E-mail: r.delf@ed.ac.uk (corresponding author); r.bingham@ed.ac.uk; andrew.curtis@ed.ac.uk
[2]University of Edinburgh, School of Engineering, Edinburgh EH9 3JL, UK. E-mail: a.giannopoulos@ed.ac.uk.

the effectiveness of the approach by applying the technique to two synthetic case studies in which full 3D models can be prohibitively large and where assumptions about the source and propagation mechanisms, which are implicit in 2D modeling, do not hold.

THEORETICAL BACKGROUND

Approaches to modeling 2D geometries

FDTD modeling is generally undertaken using Yee's algorithm (Yee, 1966; Taflove and Hagness, 2005). In brief, the algorithm involves a discretization of Maxwell's equations of electrodynamics, and an iterative propagation of a source term through time steps. The algorithm can be implemented in three dimensions or simplified to two dimensions in the TMz mode by assuming an infinitely long z-polarized dipole antenna (i.e., a line source) and crossline geometry invariance to remove invariant E and H field components (Taflove and Hagness, 2005) (Figure 1). The 2D simulations comprise a computationally quick method of modeling the response of a laterally invariant model. In practice, however, the assumption of an infinite z-polarized source is often violated due to the field logistics imposed on many GPR surveys. For example, due to the low frequencies often used in ground-based glaciological radio-echo sounding (Scott et al., 2010; Sevestre et al., 2015; King et al., 2016), lengthy dipole antennas are often towed inline to the survey direction and as such cannot be modeled accurately using 2D FDTD algorithms.

Additional issues with the 2D approach are encountered in the scaling of amplitude with traveltime. In a 3D domain with a point source, $A \propto 1/r$, where A is the amplitude and r is the distance, but in two dimensions, the source becomes an infinite dipole and the relationship becomes $A \propto 1/\sqrt{r}$ (Bleistein, 1986; Auer et al., 2013). Because of this, when 2D modeling is used, the results need to be postprocessed to obtain amplitudes that quantitatively match field data. The 2D Green's function can be transformed between 2D and an equivalent 3D function through a $\pi/4$ phase shift and an amplitude scaling using the Bleistein filter (Bleistein, 1986), expressed in the frequency domain as

$$G^{3D}(\omega) = G^{2D}(\omega)\sqrt{\frac{|\omega|}{2\pi\sigma}}\exp\left(-\mathrm{sgn}(\omega)\frac{j\pi}{4}\right), \quad (1)$$

where G^{2D} and G^{3D} are the 2D and 3D Green's functions, respectively, ω is the angular frequency, $j = \sqrt{-1}$, and $\mathrm{sgn}(\omega)$ is the signum function of ω. The term σ is a scaling factor $\sigma = cr$, where r is the distance (m) and c is the velocity of propagation (ms^{-1}). This widely used function (e.g., Deregowski and Brown, 1983; Vidale et al., 1985; Esmersoy and Oristaglio, 1988; Yang et al., 2013; Lomas and Curtis, 2019) is an asymptotic solution making the far-field assumption that distance $r \gg \lambda$, the wavelength of the signal, hence the near-field phase corrections are incorrect. The scaling function σ is commonly estimated for the first-break arrival and is often inaccurate for the cases of (1) heterogeneous media, where c and r are uncertain or complex, and (2) for later arrivals after the first break. Inaccurate amplitudes result in a degraded performance for FWI algorithms (Auer et al., 2013), resulting in more complex approaches requiring a good starting velocity model to be used (Van Vorst et al., 2014).

To overcome issues of amplitude scaling and to retrieve EM polarizations in the inline survey orientation using a 2D modeling domain, several authors have used 2.5D implementations of the Yee algorithm. These project the 3D algorithm onto a 2D plane by iterating over a series of constant wavenumbers k_z (e.g., Stoyer and Greenfield, 1976; Moghaddam et al., 1991; Xu and McMechan, 1997). This approach involves multiple easily parallelizable 2D syntheses, yet it requires a reformulation of the Yee algorithm and postprocessing of the results, meaning that they have not, to date, been readily implemented in open-access FDTD software packages.

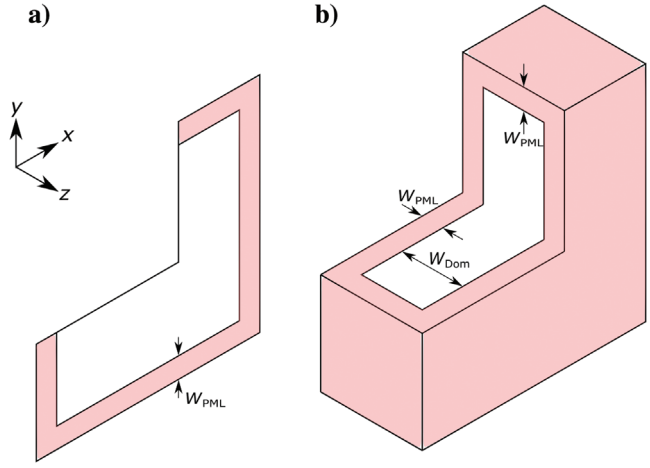

Figure 1. Schematic of (a) a 2D model and (b) a sliced-3D model, where $W_{Dom} > dx$; $W_{PML} = 15$ for both cases. Red represents the PML region, and white represents the model domain. The 2D model uses a 2D FDTD grid, whereas the sliced-3D model is a 3D FDTD domain with a minimized z-domain width, bounded on all sides by a complex frequency stretched PML.

Sliced-3D FDTD modeling

Although the preceding approaches to data preprocessing are effective in converting the processing to a 2D problem, full 3D FDTD modeling of 2D geometries remains the optimal solution for generating full 3D polarization and propagation effects (e.g., Mozaffari et al., 2016; Langhammer et al., 2017), although the computational demands of this approach can be significant. Restricting the width of a 3D domain is therefore desirable to minimize computational requirements, while retaining the benefits of 3D modeling. This we refer to as a sliced-3D approach because it uses the 3D FDTD algorithm with a laterally invariant 2D geometry, hence retaining the aforementioned correct amplitude scaling and source polarization capabilities. In the following, we show that minimizing the domain width can only be achieved through optimization of boundary conditions and that such a sliced-3D approach can show improvements over 2D modeling for near-surface GPR modeling.

PMLs

The boundaries of an FDTD grid are often terminated using a PML, in which a complex stretching function s_u is used to scale the model domain and to provide a mechanism for reflectionless signal attenuation. In the PML region, using cyclic notation $(i, j, k) \in (x, y, z), (y, z, x), (z, x, y)$ (Giannopoulos, 2018), Maxwell's equations become

DOI:10.1190/geo2020-0222.1

$$j\omega\tilde{D}_i = \frac{1}{s_j}\frac{\partial\tilde{H}_k}{\partial j} - \frac{1}{s_k}\frac{\partial\tilde{H}_j}{\partial z}, \tag{2}$$

$$j\omega\tilde{B}_i = \frac{1}{s_k}\frac{\partial\tilde{E}_j}{\partial k} - \frac{1}{s_j}\frac{\partial\tilde{E}_k}{\partial j}. \tag{3}$$

Minimizing the z-dimension of a 3D model results in energy propagating within the model domain at grazing (low-incidence) angles to the PML boundary, hence we use a complex frequency stretched PML (hereafter, CFS-PML) (Roden and Gedney, 2000; Berenger, 2002; Taflove and Hagness, 2005; Giannopoulos, 2008) where the stretching function s_u is of the form

$$s_u = \kappa_u + \frac{\sigma_u}{\alpha_u + j\omega\epsilon_0}, \tag{4}$$

where $u \in (i, j, k)$ is the orientation perpendicular to the model boundary, κ_u is a unitless quantity, which dictates a real coordinate stretch in the PML region, α is a frequency shift factor, and $\sigma/j\omega$ introduces an imaginary spatial coordinate stretch mainly responsible for signal attenuation. In this paper, we assume that the PML parameters are the same in each orientation, so we will refer to s_u, α_u, κ_u, and σ_u as s, α, κ, and σ, respectively.

The CFS-PML parameters can be tuned to improve performance over a frequency range and reduce nonphysical reflections from the PML boundary. This is done by scaling parameters α, κ, and σ through the PML, usually using an integer polynomial m. The term σ is scaled from 0 to $\sigma_{\max}$ as

$$\sigma(x) = \sigma_{\max}\left(\frac{x}{d}\right)^m, \tag{5}$$

where d is the depth of the PML in cells and $0 < x < d$ is the location within the PML so as to avoid sudden changes in σ and the associated nonphysical reflections. We use the commonly used (Gedney and Zhao, 2010; Giannopoulos, 2012) estimate of optimum $\sigma_{\max}$ after Gedney (1996) whereby

$$\sigma_{\max} \approx \frac{m+1}{150\pi dx\sqrt{\epsilon_r}}, \tag{6}$$

where m is a polynomial scaling, dx is the spatial resolution, and ϵ_r is the relative dielectric constant. The term κ is similarly often scaled from 1 to $\kappa_{\max}$ by

$$\kappa(x) = 1 + (\kappa_{\max} - 1)\left(\frac{d-x}{d}\right)^m, \tag{7}$$

such that $\kappa = 1$ (no coordinate stretch) at the model/PML interface and $\kappa = \kappa_{\max}$ at the grid boundary.

The frequency shift factor α is generally scaled from a maximum at the model/PML boundary to zero at the outermost grid boundary to minimize the reflection coefficient at the PML/model boundary (Taflove and Hagness, 2005) and provide broadband attenuation within the PML. Hence,

$$\alpha(x) = \alpha_{\max}\left(\frac{1-x}{d}\right)^m. \tag{8}$$

Higher order CFS-PMLs operate via a product of multiple contributions by

$$s = \prod_{i=1}^{N} s_i, \tag{9}$$

where N is the number of terms, i is the order, and s_i is defined in equation 4, with the aim of combining the characteristics of improved attenuation within the PML compared to the standard PML with the attenuation of evanescent energy of the CFS-PML. Typically, two terms ($N = 2$ in equation 9) are used for a higher order PML, but more terms are possible by introducing further terms of s_i. Feng et al. (2017) optimize a higher order PML for the application of broadband seismic modeling and show a reduction in the error as a result. However, it is clear from inspection that such implementations introduce cross terms in addition to the desired terms such as, for a second-order CFS-PML (Giannopoulos, 2018),

$$s = \left(\kappa_1 + \frac{\sigma_1}{\alpha_1 + j\omega\epsilon_0}\right)\left(\kappa_2 + \frac{\sigma_2}{\alpha_2 + j\omega\epsilon_0}\right). \tag{10}$$

What remains unclear is what impact these additional cross terms have in an optimization process. Along with the higher number of degrees of freedom associated with multiple stretching functions, this results in the process becoming a cumbersome problem for the general case and hence will not be considered in this study.

METHODOLOGY

We initially demonstrate the impact of using a small crossline domain size on the signal error as a result of the aforementioned evanescent energy. We demonstrate the effect of reducing the crossline domain size for a homogeneous ice ($\epsilon_r = 3.2$) model (Figure 2a) and a layered model of homogeneous ice overlying a bedrock layer ($\epsilon_r = 20$) (Figure 2b).

We then undertake a series of sensitivity experiments with uniform models to investigate the performance of PMLs in attenuating grazing wave energy on the boundary of the sliced-3D model for a sliced-3D model with a fixed domain size of 5 cells and a PML thickness of 15 cells. The experiments are performed at 25 and 50 MHz using a Ricker wavelet. We use an approach similar to that of Taflove and Hagness (2005) and Drossaert and Giannopoulos (2007) in testing parameter pairs over an expected range to derive the optimum values because, although this is a computationally intensive option, it allows a clear assessment of the sensitivity to different parameters. We initially do this using a κ scaling polynomial $m = 2$ and α polynomial $m = 1$ (see equations 7 and 8). The model is discretized at 0.1 m to give a model domain size of $24 \times 24 \times 3.5$m. The PML thickness is extended compared to a typically used 10-cell implementation, with the intention of reducing errors due to normal incidence energy at the bounding edges, which may not be attenuated as effectively when optimization is undertaken to reduce the evanescent energy. We then repeat this approach

to investigate the impact of polynomial order m for κ and α, running this test for all combinations between $m = 0$ (constant value) and $m = 6$.

We then investigate the frequency dependence of the optimal CFS-PML parameters, by doing a similar grid search parameter test as for the previous tests, but this time using an impulse source type followed by a convolution with a Ricker wavelet with central wavelength λ_c. We limit the frequencies used to $20 < \lambda_c/dx < 100$ because this is the most commonly used range of λ/dx for efficient FDTD modeling, also noting the dispersion limit of $dx < \lambda_{\min}/10$ (Giannopoulos, 1998) and that for a Gaussian waveform the minimum significant wavelength considered for dispersion (error < -40 dB) is $\lambda_{\min} \approx \lambda_c/3$. Using a grid size of 0.01 and 0.1 m, this allows testing in the range of 100–700 and 10–70 MHz, respectively. For this experiment, we use a 5-cell domain width with a 15-cell PML.

For each of these sensitivity experiments, a reference solution of a 3D model $\mathrm{E}(x, y, t)_{\mathrm{ref}}$ is calculated using a large 3D model with an identical 2D geometry, to give the response where there is no interaction with bounding PMLs normal to the z-orientation. The 3D model consists of identical geometry in the x- and y-orientations, with a 120-cell model width in the z-orientation and a 10-cell PML using a constant $\kappa_{\max} = 1$, and σ scaled linearly between 0 and $\sigma_{\max}$ after equation 6. As a result of this larger width, there is no grazing-wave interaction with the model-PML interface, and we can assume this to be the best-case scenario with a minimum error

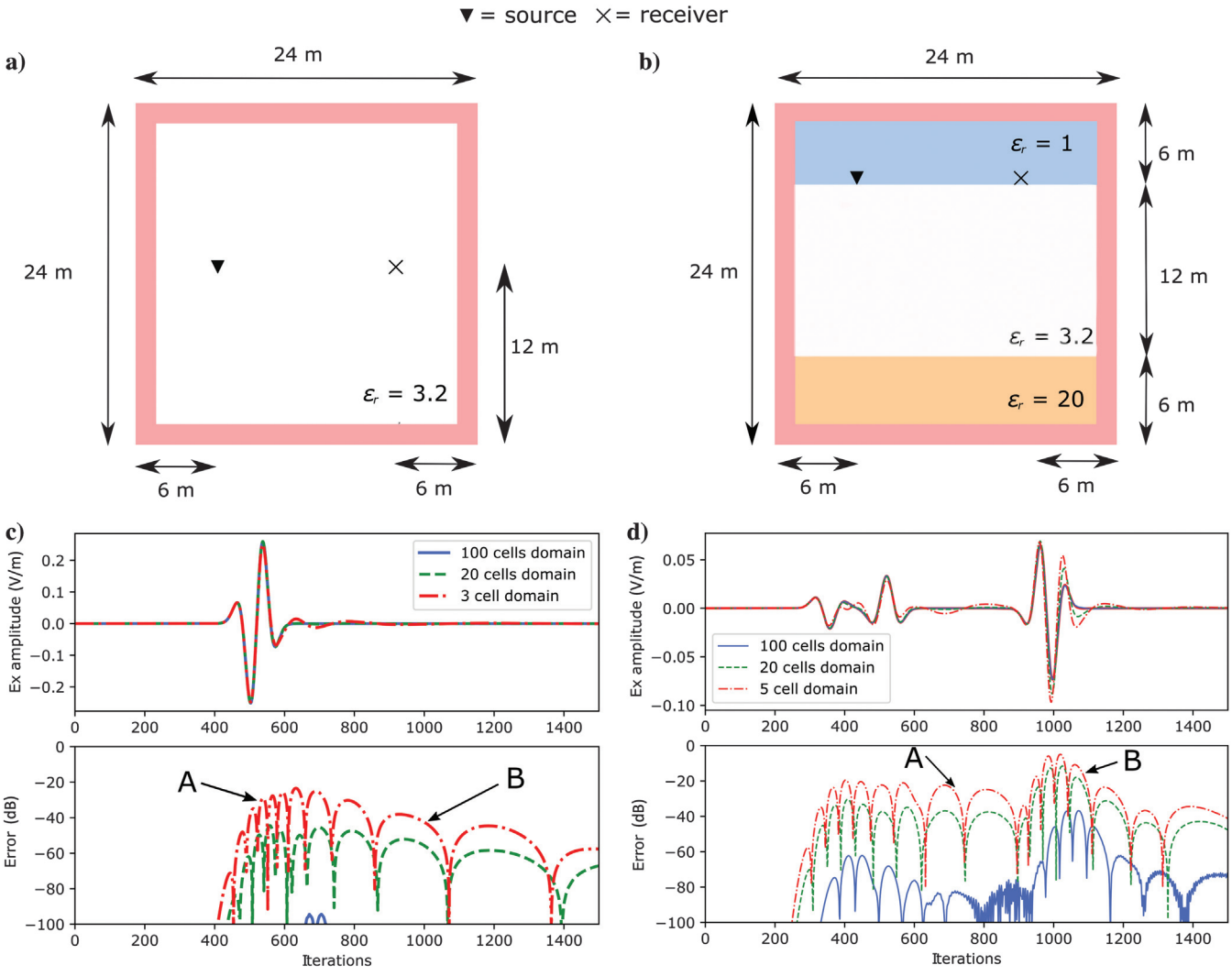

Figure 2. Comparison of the effects of crossline domain size (in/out of the page), for (a and c) a homogeneous ice ($\epsilon = 3.2$) model with a Gaussian wavelet and a standard PML and (b and d) a three-layer model with a homogeneous ice layer overlying flat bedrock with a free-space layer above the surface. Here, $dx = 0.1$ m and the PMLs are 10 cells thick. Two sources of noise can be noted for each. The A denotes high-frequency noise as a result of normal incidence reflections through the PML. The arrival time of this noise is delayed in wider implementations as the two-way traveltime between boundaries (out of the plane in [a] and [b]) increases. The B denotes low-frequency evanescent noise as a result of grazing wave interactions between the signal and the PML boundary. A wider model results in minimization of this noise because the incidence angle increases with the increasing width.

response. Errors are reported relative to this reference solution as in Roden and Gedney (2000), Berenger (2002), Taflove and Hagness (2005), Giannopoulos (2008), and Feng et al. (2017) as

$$\text{error}(x, y, t) = 20 \log_{10} \frac{\text{E}(x, y, t) - \text{E}(x, y, t)_{\text{ref}}}{\text{E}_{\text{ref}_{\text{max}}}}, \qquad (11)$$

where $\text{E}(x, y, t)$ is the output electric field in time, $\text{E}(x, y, t)_{\text{ref}}$ is the reference solution in time, and $\text{E}_{\text{ref}_{\text{max}}}$ is the maximum value of the reference solution.

To demonstrate the performance of the sliced-3D approach, we repeat our experiment of investigating domain width sensitivity to confirm that an improvement in error is observed using an optimized CFS-PML, before comparing the performance of an optimized first-order PML with those previously published in the literature, including Feng et al. (2017), which was developed for computational seismology but follows a similar theory, along with Gedney and Zhao (2010) and as outlined previously. For this case, we use a model discretization of 0.005 m and free space ($\epsilon_r = 1$).

NUMERICAL RESULTS

Impact of domain size

Figure 2 shows the results of reducing the domain size for homogeneous and layered models. Thin models (with a three-cell model domain size) show significant (> -20dB) noise levels at the signal arrival, followed by low-frequency ringing as a result of evanescent energy from the model-PML interface. Figure 3 shows the error for the x- and z-polarizations for the homogeneous ice model. We estimate an error of -40 dB (1%) to be a feasible target to reduce the errors below the signal-to-noise ratio of a typical radargram, which, from Figure 3, would require a domain width of 60 cells. At small domain sizes, the effect of evanescent energy is significant, whereby low-frequency and high-amplitude errors are introduced following the direct arrival (the arrivals in Figure 2, marked "B"). Thickening the PML has a minimal impact on this error because it is induced by the model/PML boundary.

First-order PML optimization

The optimum values for α and κ are estimated through a brute-force grid search approach, producing error contour plots exemplified in Figure 4. The grid search shows minimum error bounds of -65 and -45 dB for 25 and 50 MHz, respectively. A clear frequency dependence of the optimum parameters can be seen, indicating that the optimum κ_{max} decreases with increasing frequency and that the sensitivity of error to the α value decreases with the increasing frequency. This is intuitive because κ dictates the real coordinate stretch of the PML — a higher value results in a higher stretch, such that the maximum λ/dx within the stretched coordinates of the PML is minimized. The optimum value of α is approximately the same for both experiments, but it has a much lower sensitivity at high frequencies.

Impact of the polynomial order

Figure 5 shows the minimum error for each grid search as a function of order of polynomial scaling. It is clear that, for this example, a constant α scaling function is the most efficient, with a maximum -80 dB error. Higher orders of α result in an error of at least -50 dB. A quadratic κ scaling function is shown to provide the optimum attenuation for all orders of α. This result contrasts with Taflove and Hagness (2005), who suggest that $\alpha = 0$ at the outermost grid boundary to enable sufficient traveling wave energy attenuation. Our optimal parameter setting is therefore minimizing the effect of evanescent energy, with the remaining noise being primarily as a result of normal-incidence energy at the source point.

Frequency dependence

Figure 6 shows the minimum error and optimum α and optimum κ as a function of λ/dx, first demonstrating (Figure 6a) that the error

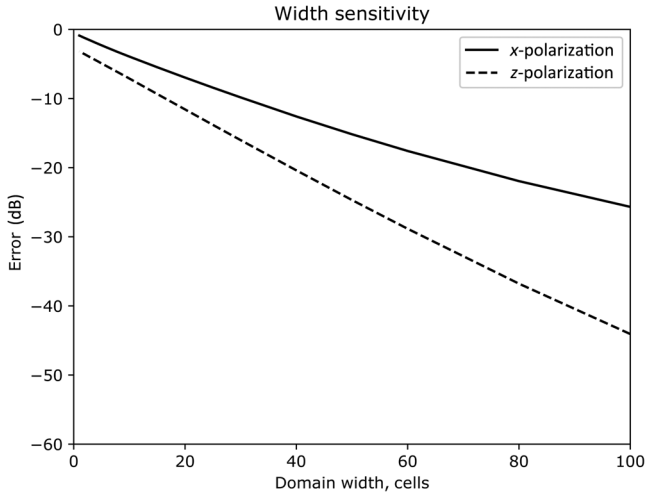

Figure 3. Plot of the maximum error as a function of the domain width for the homogeneous ice model shown in Figure 2a. Decreasing the model width results in increased error as a result of interactions with the grazing-angle incident energy.

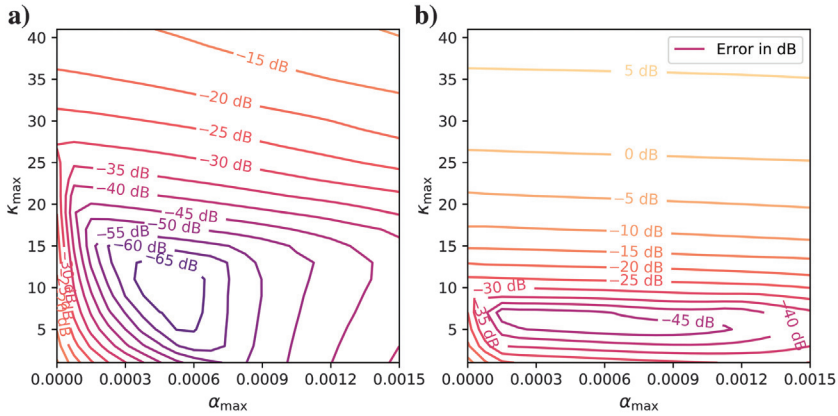

Figure 4. Contour plot of the maximum error as a function of α_{max} (the frequency shift factor, equation 4) and κ_{max} (the stretching factor) for a homogeneous ice model with a 5-cell width model domain, 15-cell first-order PMLs, with $dx = 0.1$m. A Gaussian waveform with the central frequency of (a) 25 MHz and (b) 50 MHz is used.

is relatively constant at approximately −70 dB for all values of λ/dx tested. Figure 6b shows that the optimum selection of κ is linear with λ/dx, with a linear relationship of

$$\kappa_{\max} = 0.14\frac{\lambda}{dx} - 1. \tag{12}$$

In Figure 6c, $\alpha_{\max}$ is plotted as $\log_{10}\alpha_{\max}dx$ as a function of λ/dx. A negative linear relationship can be plotted for the range $20 < \lambda/dx < 70$ of form $y = mx + c$,

$$\log_{10}(dx\alpha) = -0.005\frac{\lambda}{dx} - 4, \tag{13}$$

which reduces to

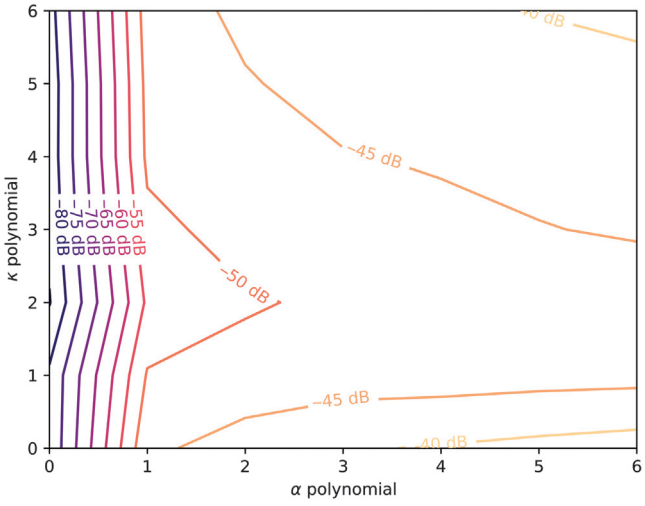

Figure 5. Minimum error for all combinations of polynomial scaling. This is found through repeating the results of Figure 4 for each combination of polynomials in α and κ. The optimum value is shown to be 0 for α and 2 for κ.

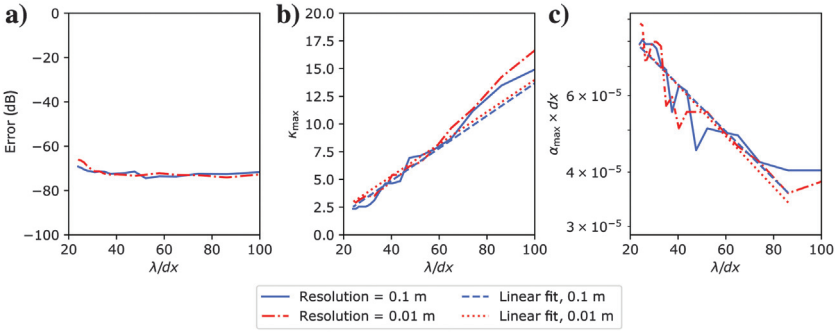

Figure 6. Frequency dependence of the first-order CFS-PML parameters using a discretization of 0.1 and 0.01 m for the homogeneous model (Figure 2a). (a) The error as a result of the optimum parameters. (b) Optimum $\kappa_{\max}$ as a function of λ/dx. A positive linear trend is observed as expected as a larger $\kappa_{\max}$ is expected for larger wavelengths. (c) The term $\alpha \times dx$ plotted as a function of λ/dx. This plot is scaled by discretization on a lin-log plot, demonstrating that the optimum α shows a slight negative trend with λ/dx and a scaling with resolution.

$$\alpha = \frac{10^{-4-0.005\frac{\lambda}{dx}}}{dx}. \tag{14}$$

Together with equation 6, these values can be readily used as a guideline for first-order CFS-PML parameters in the frequency range suggested because they only require calculation of a central wavelength λ and the discretization. As such, they can be readily calculated in the FDTD implementation. In addition, Figure 7 shows that, at higher frequencies (i.e., lower values of λ/dx), the error is much more sensitive to the value of $\kappa_{\max}$ than to the value of $\alpha_{\max}$, and this provides a more stable linear regression result in Figure 6.

Domain width revisited

With our new understanding of the optimum CFS-PML parameters, we now revisit the signal error as a function of the domain width (Figure 8). The optimized PML gives a consistent result of −38 dB for an x-polarized source type and −45 dB for a z-polarized source type. The error increases slightly at a domain width of 10 cells for a z-polarized source, but it remains under −40 dB down to a 3-cell domain width. In the following examples, we use a five-cell domain width as a balance between the computational requirements and accuracy.

Comparison of implementations

The performance of differing implementations is compared in Figure 9 using a sliced-3D homogeneous ice model as shown in Figure 2a, now using 60 receivers in the positive x-direction, representing a common-source point experiment. The difference between each result and the reference solution in Figure 9a is shown in Figure 9b–9e. This demonstrates that a correctly optimized first-order CFS-PML can produce synthetic data with no evanescent energy in a sliced-3D model domain. There is a slight error close to the source point in Figure 9c as a result of the CFS-PML's reduced ability to attenuate normal-incidence energy. Other recommendations (Figure 9d and 9e) for the CFS-PML parameters show strong evanescent energy, showing that although these have been recommended for a general case for first- and second-order CFS-PMLs, they are not suitable in this application.

EXAMPLES

Cross-borehole example

We now demonstrate the performance of sliced-3D FDTD modeling in two applications for which error levels and model computational demand are important considerations. We first use a cross-borehole survey configuration in the presence of a heterogeneous soil with ϵ_r ranging between 8 and 18. This is similar to the cross-borehole FWI experiment configurations of Ernst et al. (2007), Klotzsche et al. (2010), and the computational configuration of Mozaffari et al. (2016). We use a single z-polarized source point with a 200 MHz Ricker wavelet, with an array of

DOI:10.1190/geo2020-0222.1

receivers located in a second borehole (see Figure 10a). The source and receiver boreholes are separated by 6 m. Using a discretization of 0.02 m, the recommended parameters from equations 12 and 14 are $\alpha = 0.00397$ and $\kappa_{max} = 1.80$. We undertake the simulations in three dimensions, sliced 3D, and in two dimensions. The sliced-3D model domain consists of 1 cell width, with PMLs extended to 15 cells to minimize noise from normal-incidence energy.

All of the simulations are undertaken with a z-polarized source to enable like-for-like polarization comparison with the 2D implementation. We apply a frequency-domain Bleistein 2D-to-3D filter to the 2D data (equation 1), with r being equal to the straight-line raypath between the source and receiver for each trace and c being calculated from the root mean square (rms) value of ϵ_r from the model. We compare the results in Figure 10c and 10d, which shows a significantly lower error field for the sliced-3D approach.

Common-offset glacier survey example

Now, we apply this approach to a model of a simple glacier with a rough bed and several internal scattering points. We use model dimensions of $150 \times 100 \times 3.5$ m with a 15-cell PML thickness and resolution of 0.1 m to demonstrate the low noise level achievable with our recommendations. A dipole source with a 25 MHz Ricker wavelet is used. Given these model parameters, CFS-PML parameters are chosen to be $\alpha = 0.00046$ and $\kappa_{max} = 3.70$, following Figure 6 and equations 12 and 14. We use a single-channel common-offset survey acquisition with the source and receiver separated by 5 m to represent a typical survey with low-frequency dipole antennas. Several scattering points with $\epsilon_r = 80$ are imposed to simulate scattering bodies found within polythermal ice (Barrett et al., 2008). We use 130 source/receiver locations along the surface of a free-space/ice interface.

The results of the model are shown in Figure 11, along with the error in dB in the second row. Figure 11c shows the solution for a sliced-3D model with optimized CFS-PML parameters with the error compared to a 3D reference. This shows that optimization of PML parameters can lower the error for scattering bodies to be consistently less than −40 dB, with only some later arrivals close to the bed with the error greater than −40 dB. Figure 11e and 11f shows the response and error for a sliced-3D model with no PML optimization, respectively. Low-frequency noise is prevalent throughout, and errors at the bed are significant. Figure 11g and 11h shows the response for a 2D model with 2D-to-3D transformation with the Bleistein filter assuming a first-break time of 1 μs for the bed return (2600 iterations in Figure 11) and fails to replicate well the amplitudes for any of the scattering or bed returns.

Computationally, testing on a workstation with a four-core Intel Xeon CPU E3-1505M v5 @ 2.80GHz, the sliced-3D approach required 1.02 GB RAM and completed a single simulation in 17 min 54 s compared to the wider 3D model that required 4.06 GB RAM and completed a simulation in 74 min 18 s for the same model. This was largely driven by the reduction by a factor of four in the number of cells in the sliced-3D model.

DISCUSSION

The numerical results from the preceding examples show that the errors caused by near-grazing wave interactions with a bounding PML region can be significantly attenuated through optimization of the first-order CFS-PML parameters. We have suggested relationships between the optimal parameters and the model parameters to attenuate such low-frequency energy significantly as a function of λ/dx, which can be readily calculated using the model parameters and source frequency used.

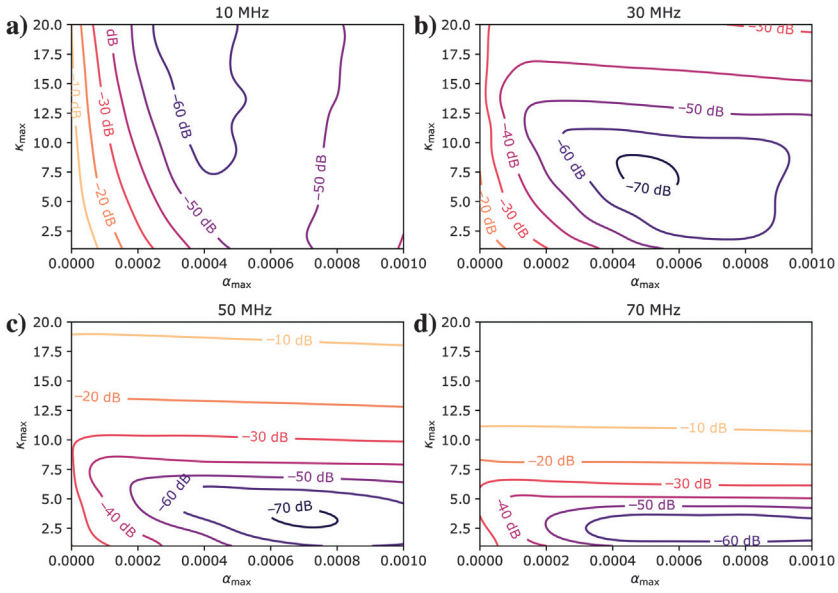

Figure 7. The error surface as a function of κ and α for (a) 10 MHz, (b) 30 MHz, (c) 50 MHz, and (d) 70 MHz, where dx = 0.01 using the same experimental setup as in Figure 6a.

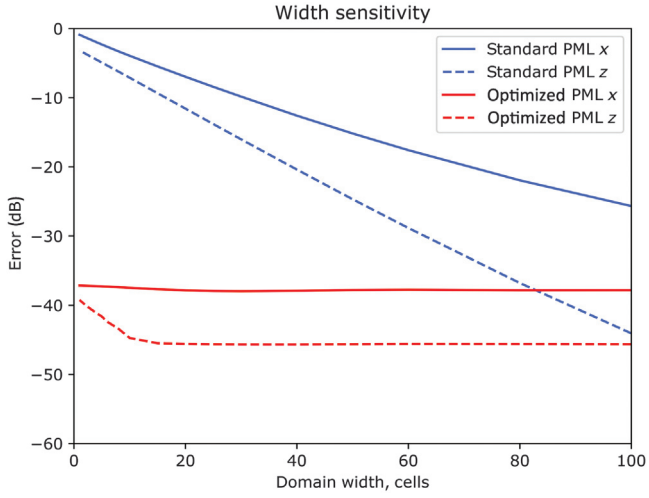

Figure 8. Comparison of the signal error as a function of the domain width, as in Figure 3, but including results with an optimized CFS-PML, using the horizontally layered model as in Figure 2c and 2d. A consistent −38 dB can be achieved for the x-polarized result, and −45 dB can be achieved for the z-polarization using our recommendations for the CFS-PML parameters.

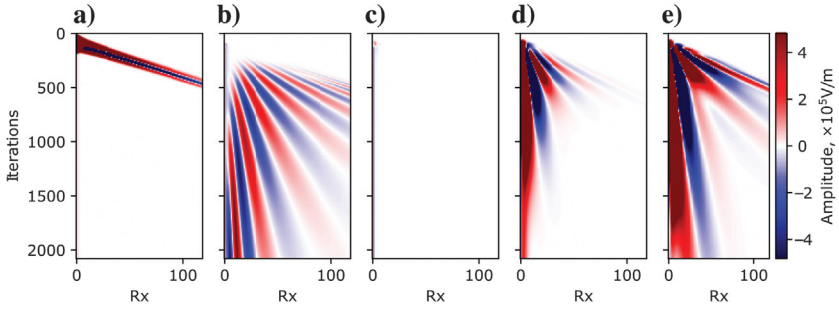

Figure 9. Error plots as a function of the receiver offset and time for a 5-cell width sliced 3D domain with a z-polarized source at 50 MHz. The error is the difference between the result and a reference 3D solution. The color scale is clipped at 1% of the maximum. (a) Reference solution from a 3D model showing the direct arrival; (b) a sliced-3D domain with no PML parameter optimization; and (c) the same model with optimum parameters selected from equations 12 and 14, (d) with parameters selected from the results of Feng et al. (2017), and (e) with the parameters recommended by Gedney and Zhao (2010). This comparison demonstrates that a well-optimized first-order CFS-PML, using recommendations from this study, can show an improvement for grazing-wave interactions over generic parameters chosen for the first- and second-order PMLs, which are often developed for different applications.

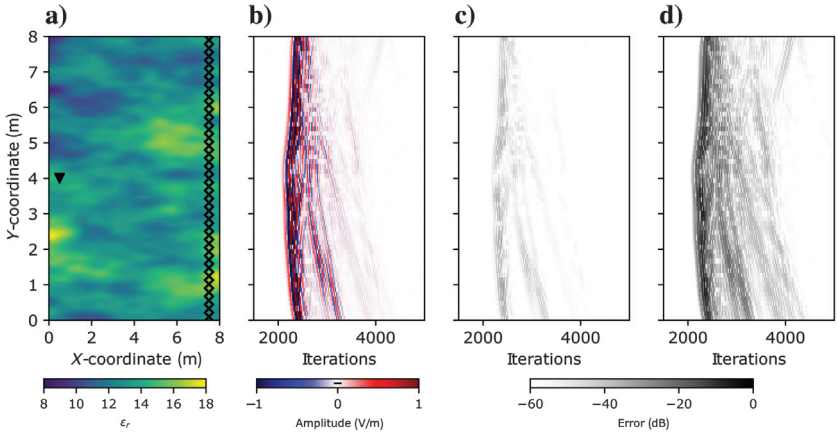

Figure 10. Cross-borehole GPR experiment example. (a) Model domain showing random variations in the dielectric constant, overlaid with the source point (the triangle) and receiver locations (the crosses). (b) Results of a full 3D modeling experiment using a z-polarized source. (c) Error plot (in dB) using a sliced-3D domain with the parameters recommended in this paper. (d) Error plot (in dB) of 3D-to-2D transformed data using a Bleistein filter.

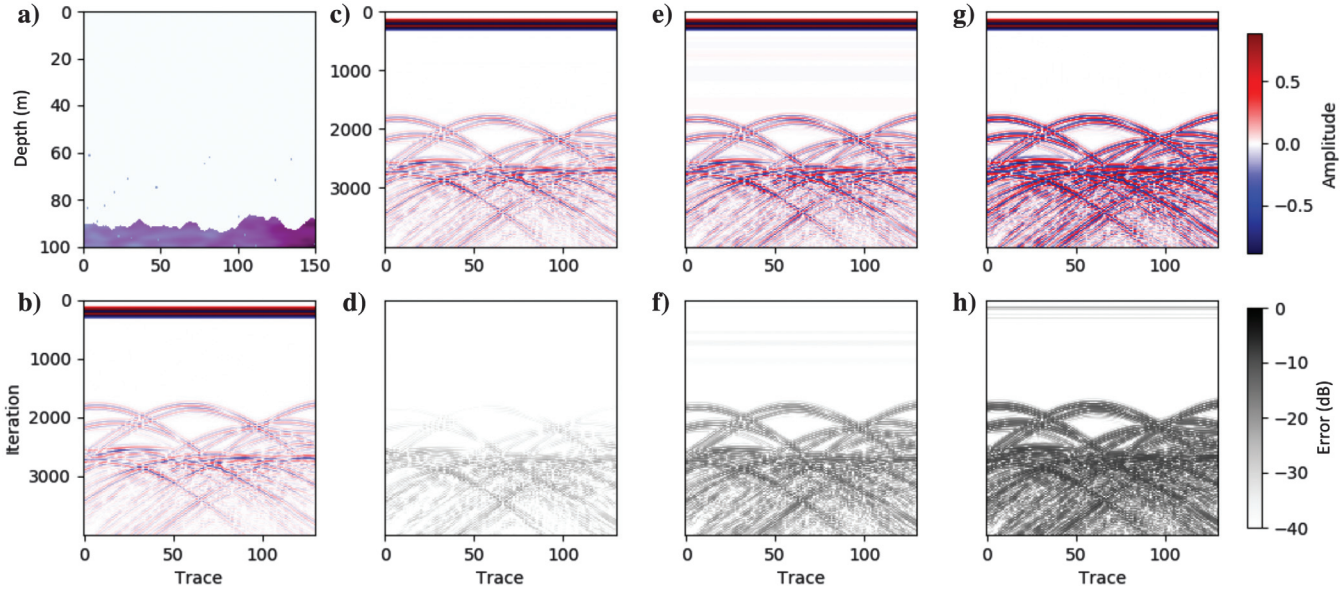

Figure 11. Synthetic model representing a glacier bed with internal scattering points within the ice. (a) Initial model with homogeneous ice and a rough bed. (b) Reference model response from the full 3D simulation. (c) Model response and (d) error with a sliced-3D domain and an optimized CFS-PML, using the recommendations from equations 12 and 14. (e) Model response and (f) error for a sliced-3D domain with no optimized CFS-PML, using $\alpha_{\max} = 0$, $\kappa_{\max} = 1$, and $\sigma_{\max} = \sigma_{\text{opt}}$. (g) Model response and (h) error for a 2D model followed by a 2D-to-3D Bleistein filter transformation. A significant improvement in error can be observed when the correct source polarization is used in a sliced-3D approach.

In practice, the effect of κ in the CFS-PML formulation is a real stretching of the cells within the PML region. Higher values of κ result in an increasing cell size within the PML region. As such, κ_{max} is a balance between larger stretch and nonattenuated dispersive effects. For larger stretch coefficients, low-frequency energy is more effectively attenuated, although large cell sizes can result in numerical dispersion at the outermost bounds of the PML introducing high-frequency noise that the PML is not effective at attenuating.

Although there have been significant developments in PML implementations through increasingly complex and higher order stretching functions, this study represents the first numerically based approach to optimize first-order CFS-PML parameters for a broad range of low-frequency geophysical applications. We have compared our results to values published in the literature (Figure 9), although it must be noted that the previous values have been derived and estimated for different applications, and as such the performance cannot always be expected to match those derived for this application.

We have suggested that our parameter choices can be applied for radioglaciological surveys, but the effects of a wider range of dielectric materials have not been explored. Regions of higher ϵ_r result in increased numerical dispersion in the propagation, resulting in the requirement of a higher resolution model. In such a case, we require improved attenuation of lower λ/dx values, which is shown in Figure 6 to result in a higher sensitivity of error on κ_{max}. This may be a limitation of the technique in applications to wider geoscientific applications of sliced-3D FDTD modeling.

Further work in this area could explore the improvements that may be attained through optimization of higher order CFS-PMLs or through optimization of recently developed multipole PML (Giannopoulos, 2018). However, such approaches will necessarily be more complex due to their implicit higher degrees of freedom.

CONCLUSION

We have shown through numerical modeling that optimization of a first-order CFS-PML can be undertaken to minimize the domain size to obtain full 3D polarization synthetics in the case of strictly 2D geometries. Such an approach is required to reduce the impact of grazing-angle evanescent energy close to the model and PML boundary. For a 5-cell domain size with a 15-cell PML, we can reach a maximum amplitude error of -70 dB (or 0.03%) over the typical range of λ_c/dx used for efficient numerical modeling. We have suggested relationships among CFS-PML parameters α, κ, and λ/dx that demonstrate the suitability of such an approach for wider applications of GPR FDTD modeling in which consideration of the waveform polarization is important. These recommendations mean that this approach is readily applicable in iterative processing algorithms because the parameters can be automatically estimated using the defined model.

ACKNOWLEDGMENTS

R. Delf and R. G. Bingham acknowledge funding from the U.K.'s Natural Environment Research Council via R. Delf's scholarship in the Edinburgh E^3 Doctoral Training Partnership (NE/L002558/1). We thank the editors and two anonymous reviewers for their helpful comments on this paper.

DATA AND MATERIALS AVAILABILITY

Data associated with this research are available and can be obtained by contacting the corresponding author.

REFERENCES

Auer, L., A. M. Nuber, S. A. Greenhalgh, H. Maurer, and S. Marelli, 2013, A critical appraisal of asymptotic 3D-to-2D data transformation in full-waveform seismic crosshole tomography: Geophysics, **78**, no. 6, R235–R247, doi: 10.1190/geo2012-0382.1.

Barrett, B. E., T. Murray, R. Clark, and K. Matsuoka, 2008, Distribution and character of water in a surge-type glacier revealed by multifrequency and multipolarization ground-penetrating radar: Journal of Geophysical Research, **113**, F04011, doi: 10.1029/2007JF000972.

Berenger, J.-P., 2002, Application of the CFS PML to the absorption of evanescent waves in waveguides: IEEE Microwave and Wireless Components Letters, **12**, 218–220, doi: 10.1109/LMWC.2002.1010000.

Bingham, R. G., D. G. Vaughan, E. C. King, D. Davies, S. L. Cornford, A. M. Smith, R. J. Arthern, A. M. Brisbourne, J. De Rydt, A. G. Graham, and M. Spagnolo, 2017, Diverse landscapes beneath Pine Island Glacier influence ice flow: Nature Communications, **8**, 1–9, doi: 10.1038/s41467-017-01597-y.

Bleistein, N., 1986, Two-and-one-half dimensional in-plane wave propagation: Geophysical Prospecting, **34**, 686–703, doi: 10.1111/j.1365-2478.1986.tb00488.x.

Busch, S., J. van der Kruk, J. Bikowski, and H. Vereecken, 2012, Quantitative conductivity and permittivity estimation using full-waveform inversion of on-ground GPR data: Geophysics, **77**, no. 6, H79–H91, doi: 10.1190/geo2012-0045.1.

Church, G. J., A. Bauder, M. Grab, S. Hellmann, and H. Maurer, 2018, High-resolution helicopter-borne ground penetrating radar survey to determine glacier base topography and the outlook of a proglacial lake: 17th International Conference on Ground Penetrating Radar (GPR), IEEE, 1–4.

Deregowski, S. M., and S. M. Brown, 1983, A theory of acoustic diffractors applied to 2-D models: Geophysical Prospecting, **31**, 293–333, doi: 10.1111/j.1365-2478.1983.tb01055.x.

Drossaert, F. H., and A. Giannopoulos, 2007, A nonsplit complex frequency-shifted PML based on recursive integration for FDTD modeling of elastic waves: Geophysics, **72**, no. 2, T9–T17, doi: 10.1190/1.2424888.

Ernst, J. R., A. G. Green, H. Maurer, and K. Holliger, 2007, Application of a new 2D time-domain full-waveform inversion scheme to crosshole radar data: Geophysics, **72**, no. 5, J53, doi: 10.1190/1.2761848.

Esmersoy, C., and M. Oristaglio, 1988, Reverse-time wave-field extrapolation, imaging, and inversion: Geophysics, **53**, 920–931, doi: 10.1190/1.1442529.

Feng, H., W. Zhang, J. Zhang, and X. Chen, 2017, Importance of double-pole CFS-PML for broadband seismic wave simulation and optimal parameters selection: Geophysical Journal International, **209**, 1148–1167.

Fisher, E., G. A. McMechan, A. P. Annan, and S. W. Cosway, 1992, Examples of reverse time migration of single-channel, ground-penetrating radar profiles: Geophysics, **57**, 577–586, doi: 10.1190/1.1443271.

Gedney, S., 1996, An anisotropic perfectly matched layer-absorbing medium for the truncation of FDTD lattices: IEEE Transactions on Antennas and Propagation, **44**, 1630–1639, doi: 10.1109/8.546249.

Gedney, S. D., and B. Zhao, 2010, An auxiliary differential equation formulation for the complex-frequency shifted PML: IEEE Transactions on Antennas and Propagation, **58**, 838-847, doi: 10.1109/TAP.2009.2037765.

Giannopoulos, A., 1998, The investigation of transmission-line matrix and finite-difference time-domain methods for the forward problem of ground probing radar: Ph.D. thesis, University of York.

Giannopoulos, A., 2008, An improved new implementation of complex frequency shifted PML for the FDTD method: IEEE Transactions on Antennas and Propagation, **56**, 2995–3000, doi: 10.1109/TAP.2008.928789.

Giannopoulos, A., 2012, Unsplit implementation of higher order PMLs: IEEE Transactions on Antennas and Propagation, **60**, 1479–1485, doi: 10.1109/TAP.2011.2180344.

Giannopoulos, A., 2018, Multipole perfectly matched layer for finite-difference time-domain electromagnetic modeling: IEEE Transactions on Antennas and Propagation, **66**, 2987–2995, doi: 10.1109/TAP.2018.2823864.

King, E. C., H. D. Pritchard, and A. M. Smith, 2016, Subglacial landforms beneath Rutford Ice Stream, Antarctica: Detailed bed topography from ice-penetrating radar: Earth Systems Science Data, **8**, 151–158.

Klotzsche, A., L. Lärm, J. Vanderborght, G. Cai, S. Morandage, M. Zörner, H. Vereecken, and J. van der Kruk, 2019, Monitoring soil water content using time-lapse horizontal borehole GPR data at the field-plot scale: Vadose Zone Journal, **18**, 190044, doi: 10.2136/vzj2019.05.0044.

Klotzsche, A., J. van der Kruk, G. Angelo Meles, J. Doetsch, H. Maurer, and N. Linde, 2010, Full-waveform inversion of cross-hole ground-penetrating radar data to characterize a gravel aquifer close to the Thur River, Switzerland: Near Surface Geophysics, **8**, 635–649, doi: 10.3997/1873-0604.2010054.

Langhammer, L., L. Rabenstein, A. Bauder, and H. Maurer, 2017, Ground-penetrating radar antenna orientation effects on temperate mountain glaciers: Geophysics, **82**, no. 3, H15–H24, doi: 10.1190/geo2016-0341.1.

Leuschen, C., and R. Plumb, 2001, A matched-filter-based reverse-time migration algorithm for ground-penetrating radar data: IEEE Transactions on Geoscience and Remote Sensing, **39**, 929–936, doi: 10.1109/36.921410.

Lomas, A., and A. Curtis, 2019, An introduction to Marchenko methods for imaging: Geophysics, **84**, no. 2, F35–F45, doi: 10.1190/geo2018-0068.1.

Moghaddam, M., E. J. Yannakakis, and W. C. Chew, 1991, Modeling of the subsurface interface radar: Journal of Electromagnetic Waves and Applications, **5**, 17–39, doi: 10.1163/156939391X00455.

Mozaffari, A., A. Klotzsche, G. He, H. Vereecken, J. van der Kruk, C. Warren, and A. Giannopoulos, 2016, Towards 3D full-waveform inversion of crosshole GPR data: 16th International Conference on Ground Penetrating Radar (GPR), IEEE, 1–4.

Roden, J. A., and S. D. Gedney, 2000, Convolution PML (CPML): An efficient FDTD implementation of the CFS-PML for arbitrary media: Microwave and Optical Technology Letters, **27**, 334–339, doi: 10.1002/1098-2760(20001205)27:5<334::AID-MOP14>3.0.CO;2-A.

Scott, J. B., A. M. Smith, R. G. Bingham, and D. G. Vaughan, 2010, Crevasses triggered on Pine Island Glacier, West Antarctica, by drilling through an exceptional melt layer: Annals of Glaciology, **51**, 65–70, doi: 10.3189/172756410791392763.

Sevestre, H., D. I. Benn, N. R. J. Hulton, and K. Baelum, 2015, Thermal structure of Svalbard glaciers and implications for thermal switch models of glacier surging: Journal of Geophysical Research: Earth Surface, **120**, 2220–2236.

Stoyer, C. H., and R. J. Greenfield, 1976, Numerical solutions of the response of a two-dimensional earth to an oscillatory magnetic dipole source: Geophysics, **41**, 519–530, doi: 10.1190/1.1440630.

Taflove, A., and S. C. Hagness, 2005, Computational electrodynamics: The finite-difference time-domain method: Artech House.

Van Vorst, D. G., M. J. Yedlin, J. Virieux, and E. S. Krebes, 2014, Three-dimensional to two-dimensional data conversion for electromagnetic wave propagation using an acoustic transfer function: Application to cross-hole GPR data: Geophysical Journal International, **198**, 474–483, doi: 10.1093/gji/ggu111.

Versteeg, R. J., 1993, Sensitivity of prestack depth migration to the velocity model: Geophysics, **58**, 873–882, doi: 10.1190/1.1443471.

Vidale, J., D. V. Helmberger, and R. W. Clayton, 1985, Finite-difference seismograms for SH waves: Bulletin of the Seismological Society of America, **75**, 1765–1782.

Virieux, J., and S. Operto, 2009, An overview of full-waveform inversion in exploration geophysics: Geophysics, **74**, no. 6, WCC1–WCC26, doi: 10.1190/1.3238367.

Warren, C., A. Giannopoulos, and I. Giannakis, 2016, gprMax: Open source software to simulate electromagnetic wave propagation for ground penetrating radar: Computer Physics Communications, **209**, 163–170, doi: 10.1016/j.cpc.2016.08.020.

Xu, T., and G. A. McMechan, 1997, GPR attenuation and its numerical simulation in 2.5 dimensions: Geophysics, **62**, 403–414, doi: 10.1190/1.1444151.

Yang, X., A. Klotzsche, G. Meles, H. Vereecken, and J. Van Der Kruk, 2013, Improvements in crosshole GPR full-waveform inversion and application on data measured at the Boise Hydrogeophysics Research Site: Journal of Applied Geophysics, **99**, 114–124, doi: 10.1016/j.jappgeo.2013.08.007.

Yee, K., 1966, Numerical solution of initial boundary value problems involving Maxwell's equations in isotropic media: IEEE Transactions on Antennas and Propagation, **14**, 302–307, doi: 10.1109/TAP.1966.1138693.

Yilmaz, Ö., 2001, Seismic data analysis: SEG.

Biographies and photographs of the authors are not available.